Acta Materialia 215 (2021) 117071

Contents lists available at ScienceDirect

Acta Materialia

journal homepage: www.elsevier.com/locate/actamat

Full length article

Evaluation of the influence of B and Nb microalloying on the microstructure and strength of 18% Ni maraging steels (C350) using hardness, spherical indentation and tensile tests

Sepideh Parvinian[a], Daniel E. Sievers[b], Hamid Garmestani[a], Surya R. Kalidindi[a,c,*]

[a] School of Materials Science and Engineering, Georgia Institute of Technology, 801 Ferst Dr. NW Atlanta GA 30332, USA
[b] Boeing Research and Technology, Ceramics, Extreme Environments & Metals, Huntsville, AL 35824, USA
[c] George W. Woodruff School of Mechanical Engineering, Georgia Institute of Technology, Atlanta, GA 30332, USA

ARTICLE INFO

Article history:
Received 2 February 2021
Revised 14 May 2021
Accepted 5 June 2021
Available online 11 June 2021

Keywords:
Maraging steels
Microalloying
Niobium
Boron
Spherical microindentation
High-throughput
Yield strength

ABSTRACT

Microalloyed steels with very small amounts of B and/or Nb are expected to enhance their mechanical properties. In the present work, we have designed and conducted experimental assays for evaluating the merits of microalloying 18% Ni maraging steels with small amounts of B and Nb. The experiments included the synthesis of small volumes of material with the desired compositions (labeled base alloy, alloy I, and alloy II), aging heat treatments, and mechanical property evaluation using a combination of Vickers hardness, spherical indentation stress-strain protocols, and standardized tensile tests. The microstructures of the alloys were studied using SEM/EDS, EBSD, and X-ray diffraction (XRD). The results of this study have demonstrated that the microalloyed steels with B and Nb delayed the coarsening of precipitates and retained their peak aged strength over longer exposure times in the aging process. Furthermore, comparing the estimates from hardness and the spherical indentation stress-strain protocols with the standardized tensile tests indicated that the spherical indentation protocols provided highly reliable estimates of the tensile yield strengths at significantly lower cost and effort. This study has confirmed the viability of utilizing the spherical indentation stress-strain protocols for the rapid exploration of materials composition and process spaces.

1. Introduction

Maraging steels with an outstanding combination of high strength and toughness have attracted considerable attention in aerospace applications. These special class of high-strength steels have low carbon content (0.03 wt%) and therefore demonstrate good weldability and formability in as annealed condition and thermal stability under repeated heating and cooling cycles in service [1–4]. Their superior strength, unlike other steels strengthened by carbide intermetallic, arises from the very fine and uniformly dispersed Ni-rich precipitates Ni_3 (Ti, Mo) and Fe_2Mo or Fe_2Ni (laves phases at the later stage of aging), which form after solution annealing (austenitization) and subsequent aging treatment (precipitation hardening) [5–9]. The chemical composition, size, morphology, and volume fraction of precipitates in maraging steels are highly sensitive to the initial chemical composition of the alloy and the heat treatment processes applied [3,9,10]. Often, a rigorous investigation of the chemical composition of the nanoscale precipitates requires the use of a combination of advanced characterization techniques such as transmission electron microscopy (TEM) and atomic probe tomography (APT) [1,7–9].

Several strategies have been explored in literature [11–16] to improve the properties and performance characteristics of maraging steels at room and elevated temperatures, while maintaining low production costs, especially for applications where a high strength to weight ratio is essential. A promising strategy involves microalloying with elements such as Ti, V, B, and Nb to achieve improved properties (e.g., strength, toughness, fatigue life) through grain refinement, transformation control, and precipitation hardening. In the present work, we will specifically explore the potential of improving the properties of 18% Ni maraging steels (C350) by microalloying with both B and Nb. In prior work, the microalloying effects of B and/or Nb have been studied in a variety of high-carbon steels [17,18], mild steels [14,15,18,19], and high-strength low-alloy steels (HSLA) [18,20,21]. Nb has been reported to play a critical role in strengthening via solid solution strengthening,

* Corresponding author at: George W. Woodruff School of Mechanical Engineering. Georgia Institute of Technology, Atlanta GA 30332, USA.
E-mail address: surya.kalidindi@me.gatech.edu (S.R. Kalidindi).

https://doi.org/10.1016/j.actamat.2021.117071
1359-6454/

grain refinement, and/or carbide precipitation in steel alloys [17–20,22]. The addition of B, on the other hand, is found to significantly improve the hardenability of low-carbon steel alloys without causing degradation in ductility [23–25]. It is also reported that B combined with Nb can retard recrystallization of austenite by increasing the recrystallization temperature in low-carbon steels and enhance the mechanical properties [19]. The microalloying effects of combined Nb and B on the mechanical properties of maraging steels are, however, not yet well understood.

Evaluation of the effects of chemistry and process history on the effective properties of metallic alloys demands considerable experimental effort. High-throughput assays represent an important toolset for this task, and have been the focus of several recent reports in literature [26–31]. As a prime example, Rapid Alloy Prototyping (RAP) [32] comprising sequential steps of semi-continuous casting with varying compositions, forming, heat treatment, and tensile testing was shown to be more cost-effective compared to conventional alloy design practices. One of the main bottlenecks in these efforts comes from the need to perform standardized tests (e.g., tension tests) to evaluate the mechanical properties of candidate alloy samples produced with intentional variations in chemical compositions and process histories. The standard tests incur significant costs in sample preparation and require a substantial amount of material in each chemical composition and process history being evaluated. Clearly, there is a need to develop and utilize high throughput and reliable protocols for rapid evaluation of the mechanical response of small volume samples produced in various materials development efforts.

Indentation has been commonly used in prior literature [33–36] for estimating the mechanical response of materials in small sample volumes. These methods focus mainly on the values of hardness evaluated using a sharp indenter (Vickers or Berkovich) [37–41]. The hardness values measured by a sharp indenter exhibit high sensitivity to the applied load/displacement (referred to as the indentation size effect) [42–46]. This makes it difficult to transform the hardness values reliably into estimates of properties obtained in the standardized tension tests. As a result, there is considerable uncertainty when one uses hardness values to guide the materials development efforts, which are typically aimed at achieving a certain combination of properties measured in standardized tests. Recent advances in the spherical indentation stress-strain protocols (ISS) [47,48] have now made it possible to reliably transform the load-displacement measurements in indentation on metal alloy samples to the more familiar stress-strain responses measured in tension tests. The ISS protocols can be performed at different length scales using different spherical indenter tip sizes [49]. When performed at length scales where the indentation zone involves multiple grains, these are referred to as spherical microindentation stress-strain protocols (MSS). These protocols provide reliable estimates of Young's modulus and yield strength of the sample using suitable scaling factors [50,51] that account for many of the main differences in the stress and strain states in the indentation tests compared to the tension tests.

The objective of the present work is to demonstrate the viability and the validity of spherical microindentation stress-strain (MSS) protocols for rapid evaluation of the mechanical properties of 18% Ni maraging steels (C350) microalloyed with B and Nb while using only small specimen volumes. Specifically, the effects of B and Nb microalloying on the peak aging strength of maraging steels were studied using the MSS protocols. The estimates of tensile yield strengths from MSS protocols are critically validated with direct measurements using tension tests for selected sample conditions. It is demonstrated that the MSS protocols provide higher fidelity estimates of the tensile yield strength compared to the estimates from the traditional hardness tests and produce significant savings in time and cost compared to the standardized tension tests. Wherever relevant, microscopy (SEM/EBSD) and X-ray diffraction techniques were used to study the evolution of microstructures of the different samples tested in the study.

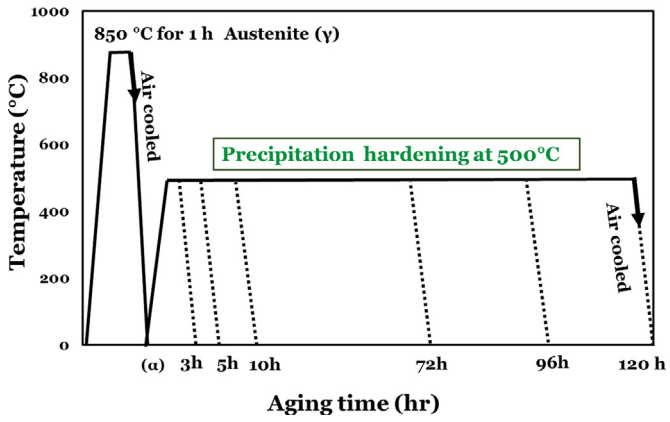

Fig. 1. Schematic of the thermal history for the maraging steel samples produced for this study. The samples after quenching in as-annealed condition acquire a fully martensitic structure (α). Alloys were age hardened at six different aging time intervals and air cooled.

2. Experimental procedures

2.1. Materials and sample prototyping

18% Ni maraging steels (C350) without the addition of B and Nb (henceforth referred to as the base alloy) and with varying contents of B and Nb (henceforth referred to as alloy I and alloy II) were produced through Vacuum Induction Melting (VIM) by Carpenter Technology, Philadelphia, PA. The chemical compositions of these alloys were measured using LECO spectrometer and X-ray methods and are listed in Table 1. The as-cast ingots (160 X 90 X 90 mm) were homogenized and compressed in a forging press at a temperature of 1000 °C in multiple passes to a final cross-sectional area of about 25×25 mm^2. Samples of dimensions 15 x 15 x 6 mm were electrical discharge machined (EDM) from the forged material along the central plane perpendicular to the forging axis. The cut samples were then solution annealed at austenitization temperature of 850 °C for 90 min in the furnace and air cooled. At this solution annealing temperature, maximum homogenization rate (diffusion-controlled) could be achieved without degradation in the mechanical properties of the forged alloys [52,53]. The annealed samples acquired a fully martensitic structure (α) upon cooling to room temperature. In order to study the influence of alloying elements on aging kinetics and the peak-aged strength of maraging steels, precipitation hardening was carried out at a selected temperature of 500 °C. This particular aging temperature was selected based on prior studies on the commercial 18% Ni maraging steels (350) [54]. The specimens of each alloy were aged to six different time periods of 3, 5, 10, 72, 96 and 120 h as depicted in Fig. 1 to cover the different regimes of underaging, peak-aging, and over-aging. This resulted in a total of 21 small volumes of sample conditions with varying processing and chemistry. The specimens were prepared for both indentation and microstructure characterization using standard metallography protocols that included grinding with silicon carbide paper down to grade 2400 and polishing successively with diamond suspensions of 3 and 1 μm. Samples were further polished with 0.04-micron colloidal silica slurry for 20 min. The as-annelaed samples were etched with an acidic ferric chloride solution for 5 s to reveal the microstructures.

Table 1
Measured chemical composition of hot-forged 18% Ni-350-grade maraging steels used in this study.

Elements (Wt%)	C	Mn	Al	Co	Fe	Mo	Ni	B	P	S	Si	Ti	Nb	Cr
Base	0.03	0.1	0.1	12	63	4.8	18.5	0	0.01	0	0.1	1.4	0	0.01
Alloy I	0.03	0.1	0.1	12	63	4.8	18.5	0.004	0.01	0	0.1	1.4	0.15	0.01
Alloy II	0.03	0.1	0.1	12	63	4.8	18.2	0.013	0.01	0.01	0.1	1.4	0.3	0.02

2.2. Microstructure characterization

Microstructure characterization was carried out using a TESCAN MIRA3 scanning electron microscope with a field emission gun. Backscattered-Electron (BSE)/SEM micrographs and EDS (energy dispersive spectroscopy) maps were collected at an operating voltage of 20 kV and 15 kV, respectively. EBSD (electron backscatter diffraction) maps with dimensions of 75×75 μm^2 were collected at an operating voltage of 20 kV with a step size of 2 µm. Phase analysis was performed by XRD technique in a PANalytical Empyrean diffractometer with Cu Kα radiation and a diffracted beam monochromator powered at 45 kV and 40 mA for scan angles (2θ) between 40° to 100°. The scanning step size and the acquisition rate were set at 0.01° and 0.0025°/s, respectively. After removing the background and normalizing the intensity, the volume fraction of austenite was determined in all samples by the widely used direct comparison method of martensite and austenite integrated intensities according to ASTM E975 [55]. This method provided reliable results under the assumption that the volume fraction of precipitates is negligible. All austenite and martensite peaks were considered in the volume fraction calculations to reduce bias errors produced by the presence of crystallographic texture.

2.3. Methods for characterization of mechanical properties

2.3.1. Tensile test and hardness test

Standard tensile specimens were prepared from selected aged steel bars in a direction parallel to the initial forging direction (FD) with a gauge diameter and gauge length of 9.7 mm and 31 mm, respectively. All tensile bars were solution annealed at 850°C for 60 min in the furnace followed by air cooling, and then aged at 500°C for 3 and 10 h followed by air cooling. Tensile tests were performed according to ASTM E8. All tests were run at room temperature maintaining the desired strain rate of 10^{-4} s^{-1} to failure. Four tensile tests were conducted and averaged for the as-annealed and aged (500 °C-3 h, air-cooled and 500 °C-10 h, air-cooled) conditions for each alloy to establish statistical relevance while maintaining lower sample preparation cost. The hardness of each specimen was assessed using a Leco Hardness Tester with a load of 1 kgf and a dwell time of 20 s. A total of 10 hardness measurements were collected for each sample condition.

2.3.2. Spherical microindentation stress-strain protocols

Spherical microindentation protocols capable of extracting the material's bulk mechanical response, where the indentation zone size can encompass several grains (about 40-100 blocks of martensite in this work) has been recently demonstrated [26,51,56]. The microindentation tests in this study were performed on a customized Zwick-Roell Z2.5 hardness tester with the indentation axis parallel to the forging direction (FD). The top and back surfaces of the samples were polished parallel to each other and fixed on a rigid surface under indenter to avoid any misalignment or sample slip. All indentation tests were run at a constant crosshead speed of 0.1 mm/min with intermittent unloading (50–30% of the peak load) and reloading cycles. Each unloading permits an estimation of a data point on the indentation stress-strain response of the material (discussed in detail later). A minimum of 7 unloading cycles was introduced in each test with load increments of 10 N between the different unloading cycles. A total of six indentation tests were carried out at randomly selected locations on each sample, while maintaining a 2 mm distance from the edge of the sample. The indentations were carried out using a spherical tungsten-carbide tip with a 500 µm radius. The collected load-displacement data was converted to indentation stress-strain responses using the protocols described next.

The indentation data analysis protocols are largely based on Hertz's theory [57], which analyzes the elastic contact between two isotropic and homogeneous bodies. This theory correlates the indentation load, P, and the elastic indentation depth, h_e, through the effective isotropic modulus, E_{eff}, and the effective radius, R_{eff}, of the combined indenter-sample system as

$$P = \frac{4}{3}\, E_{eff} R_{eff}^{1/2} h_e^{3/2} \tag{1}$$

$$\frac{1}{E_{eff}} = \frac{1-\nu_s^2}{E_s} + \frac{1-\nu_i^2}{E_i} \tag{2}$$

$$\frac{1}{R_{eff}} = \frac{1}{R_i} + \frac{1}{R_s} \tag{3}$$

$$a = \sqrt{R_{eff}\ h_e} \tag{4}$$

where (Es, vs, R_s) and (Ei, v_i, R_i) refer to Young's modulus, Poisson ratio and radius of the sample and the indenter, respectively, and a denotes the contact radius.

In our earlier work [48,51], the importance of the "zero-point" corrections identifying the effective initial contact between the indenter and the sample have been emphasized. The zero-point corrections also account for any artifacts created at the initial contact (e.g., surface roughness and oxide layer). An example of one single microindentation measurement performed in this study is summarized in Fig. 2. The main correction required in microindentation measurements is the zero-point displacement correction (h^*) and often there is no need to correct for the load. This is because when using larger indentation tip sizes of 500 µm, the microindentation measurements become less sensitive to the effects of surface roughness, oxide layers, and disparities in tip geometry. The value of this correction is identified by fitting the raw measured displacement, $\tilde{h}_e$, in the initial elastic loading regime (see the magenta segments in Fig. 2(a) and (b)) to Eq. (1), recast as

$$\left(\tilde{h}_e - h^*\right) = k(P)^{2/3} = \left(\frac{3}{4}\frac{1}{E_{eff}}\frac{1}{\sqrt{R_{eff}}}\right)^{2/3} (P)^{2/3} \tag{5}$$

where the values of k and h^* are estimated using standard linear regression analyses. Note that the load and unload segments for this first fully elastic cycle (the magenta segment in Fig. 2(a) and (b)) lie right on top of each other, confirming that this is indeed an elastic load-unload segment. In this initial elastic cycle, the effective radius R_{eff} (see Eq. (3)) is the same as the indenter radius R_i, i.e., $R_{eff} = R_i$. Therefore, one can estimate a value of E_{eff} from the value of k obtained from using Eq. (5). The sample elastic modulus, E_s, can then be estimated from Eq. (2) using Poisson ratios of 0.3 and 0.21 for the specimen and the indenter, respectively. The tungsten carbide indenter had a Young's modulus of 640 GPa in our experimental set-up.

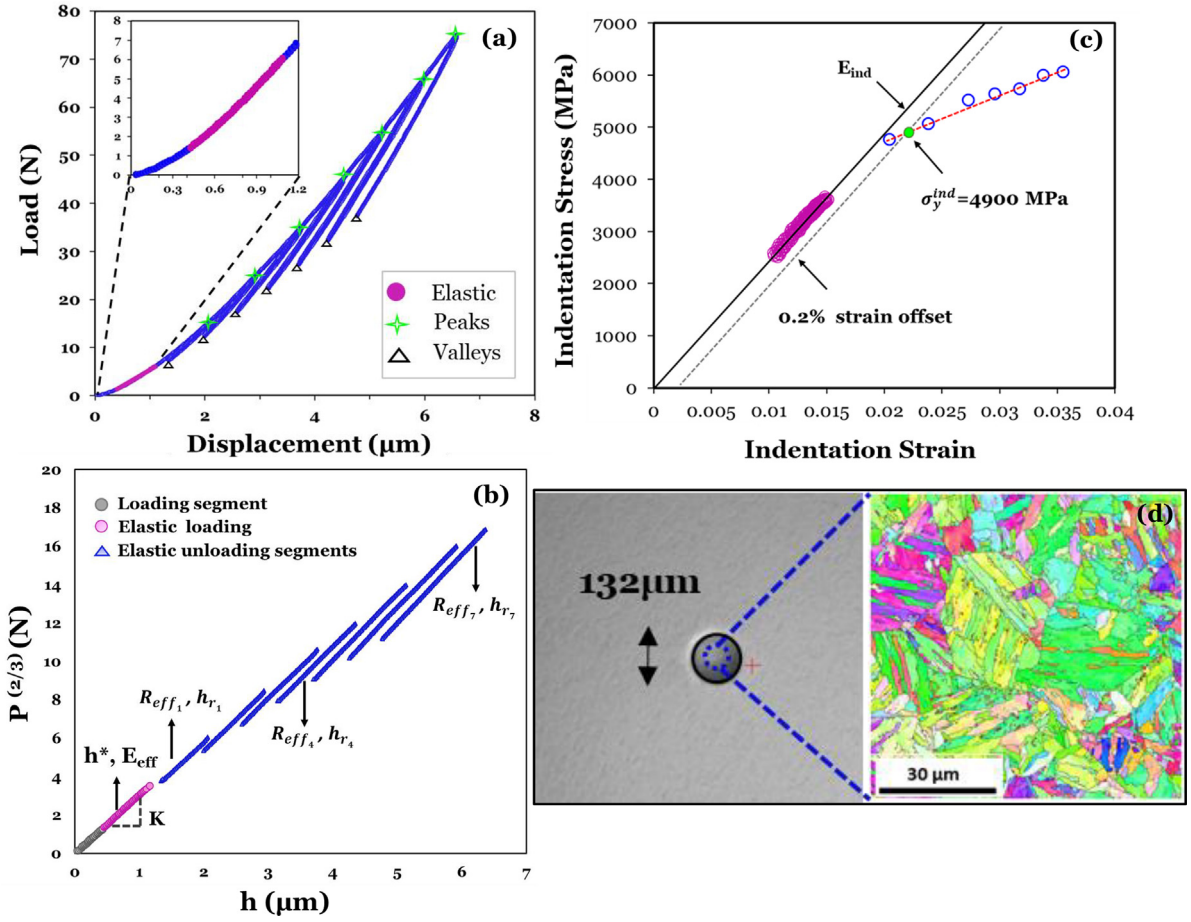

Fig. 2. (a) An example of microindentation load-displacement curve showing multitudes of load-unload cycles. The inset shows an initial elastic segment highlighted in magenta. (b) Example of linear regression analysis on the elastic unloading segments of $P^{(2/3)}$ vs. (h) to identify effective point of contact, h* (zero-point displacement correction) and the evolving R_{eff}. (c) Indentation stress-strain (ISS) curve extracted from load-displacement data after zero-point displacement correction is applied. Each post-elastic point on the ISS curve corresponds to an individual unload cycle in the load displacement measurement. (d) An optical micrograph of the specimen after unloading showing the indentation imprint, and the estimated size of the contact area at yield (dashed-line circle, 2a=66μm) equivalent to the size of EBSD image.

As the material undergoes plastic deformation, R_{eff} is no longer the same as R_i and the total displacement into the surface, h, would be the sum of the elastic displacement, h_e, and the permanent (residual) displacement, h_r. It should be noted that while R_{eff} evolves during deformation, E_{eff} is assumed to remain constant even after plasticity initiates. Since each unloading segment in Fig. 2(a) is primarily elastic, it can be analyzed using Hertz theory to estimate the values of R_{eff} and h_r corresponding to the point on the loading segment where the unloading segment was introduced. This is important because knowledge of R_{eff} and h_r allows us to estimate the contact radius at that point on the loading segment, which in turn allows estimation of the indentation stress and strain values. This set of estimations are performed by first fitting a portion of the unloading segment (selected between 85 and 50% of the peak load; see blue unloading segments in Fig. 2(b)) to the following expression using standard linear regression methods:

$$h - h_r = k(P)^{2/3} = \left(\frac{3}{4}\frac{1}{E_{eff}}\frac{1}{\sqrt{R_{eff}}}\right)^{2/3}(P)^{2/3} \tag{6}$$

The above analyses produce estimates of R_{eff} and h_r (E_{eff} was already estimated from the initial elastic segment). The contact radius at any point on the unloading segment can then be estimated using Eq. (4) as

$$a = \sqrt{R_{eff}(h - h_r)} \tag{7}$$

Specifically, our interest here is in estimating the contact radius at the point on the loading segment where the unloading was initiated. Once the contact radius for this point is estimated, the corresponding indentation stress (σ_{ind}) and indentation strain (ε_{ind}) are estimated as

$$\sigma_{ind} = \frac{P_{max}}{\pi a^2}, \varepsilon_{ind} = \frac{4}{3\pi}\frac{h}{a} \tag{8}$$

where P_{max} is the value of the load where the unloading segment was introduced. The rationale for the definitions of the indentation stress and the indentation strain presented in Eq. (8) has been discussed extensively in prior work. They can be interpreted as averaged values of the stress and strain under the indenter, and have been validated extensively [50,51,58,59]. Fig. 2(c) presents the set of indentation stress and indentation strain values extracted from the load-displacement data shown in Fig. 2(a). Note that each unloading segment leads to only one data point on the microindentation stress-strain (MSS) response. From this MSS curve, the indentation modulus is estimated as the slope of the elastic portion, and the indentation yield strength is estimated using a 0.2% offset indentation strain definition, as shown in Fig. 2(c).

The estimated sizes of the indentation zones both at yield (dashed-line circle) and at the end of the indentation test (solid circle) are illustrated in Fig. 2(d). The EBSD images shown in Fig. 2(d) roughly correspond to the indentation zone size at indentation yield. It is clear that this indentation zone includes several pre-austenite grains and martensite packets and blocks, suggesting

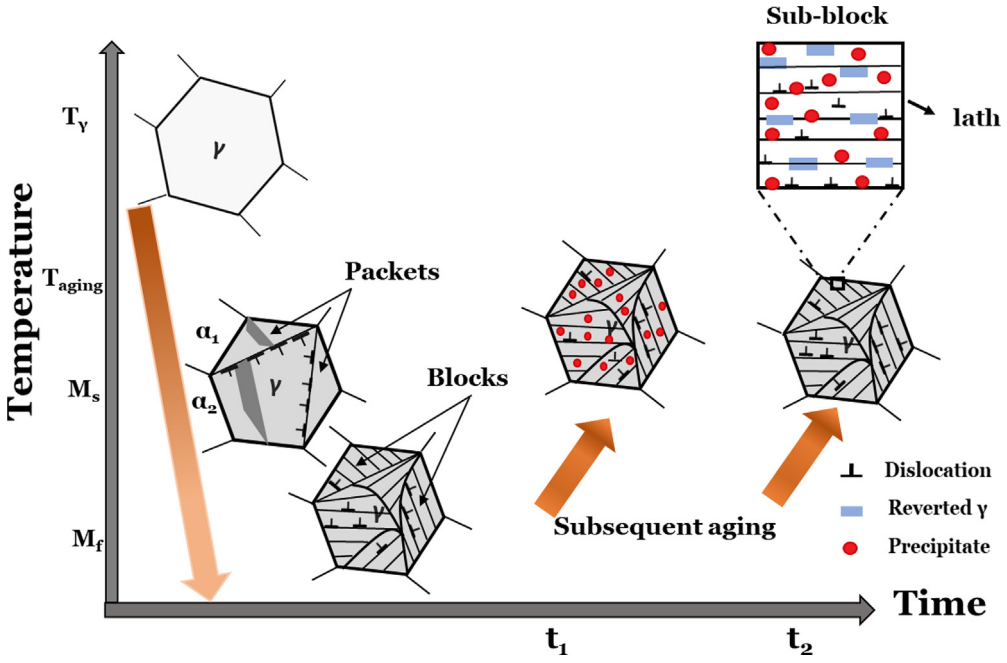

Fig. 3. Schematic of formation and evolution of martensite microstructure in one prior austenite grain after quenching and subsequent aging. The microstructure consists of packets, blocks , sub-blocks and laths in prior austenite grains. M_s and M_f denote martensite start and finish temperatures, respectively. At (T_{aging} ,t_1) precipitation takes place preferentially on dislocations and within the lath martensite to produce a fine uniform distribution of coherent particles (hardening stage). The inset shows the formation of reverted austenite and coarsening of precipitates occur simultaneously at prolog aging time, t_2 (softening stage).

that the estimated value of the indentation yield can be assumed to reflect the bulk (effective) mechanical response of the sample.

3. Results and discussion

3.1. Microstructure characterization and quantification

A schematic of martensitic transformation and the evolution of the microstructure in maraging steels after cooling from the austenite phase and during subsequent aging is presented in Fig. 3. The microstructure of martensite can exhibit a five-level hierarchy in its morphology which includes prior austenite grains, packets within pre-austenite grains, blocks within packets, sub-blocks within blocks, and fine laths within blocks [60]. The large number of interfaces and the high dislocation density (about $10^{15}m^{-2}$) present in these structures provide the necessary nucleation sites for both precipitation of intermetallic particles during the aging process (temperature range between 400–550 °C) [1,8,10] and the reversion of metastable martensite to the austenite phase after prolonged aging [1,8,61–64]. The precipitation reactions occur much more rapidly than the reversion transformation producing austenite. Thus, substantial hardening can be produced before reversion occurs. The strength of maraging steels, therefore, is controlled by the many aspects of microstructure evolution during aging, which includes precipitation, coarsening of microstructure as well as precipitates, and formation of ductile reverted austenite.

Two main microstructure features are studied in the present work: (i) packet/block size of low-carbon martensite [65,66] characterized by high angle grain boundaries (HAGBs), and (ii) austenite phase fraction. These studies were performed using BSE-SEM, EBSD imaging protocols and XRD. The morphology of martensite packets and blocks can be seen in the BSE-SEM micrographs of the base alloy, Alloy I, and Alloy II samples in the as-annealed conditions, as shown in Fig. 4(a–c). As one can see, the blocks have been transformed from an equiaxed morphology to more of a needle shape with the addition of Nb and B structure. This change can be accompanied by a change in the austenite to martensite transformation temperature (M_s) [67,68]. Fig. 4(d–f) show the EBSD produced IPF (inverse pole figure) maps showing packets and blocks (effective grain size in low carbon martensite) in the 3 different alloys exhibiting high-angle grain boundaries (with misorientations higher than 15° [69]). The packet and block size distributions shown in Fig. 4(g–i) were computed from the EBSD maps using the chord length distribution (CLD) protocols developed in prior work [70]. A large sample of chords (~ 10^6) were obtained covering directions in the range $0° \leq \theta < 180°$ with 3° intervals, and the mean intercept length was calculated.

The influence of Nb and B microalloying elements on the microstructure of hot forged and as-annealed maraging steels can be seen by comparing the alloy I and the base alloy microstructures. It is seen that the average size has reduced from 3.4 μm in the base alloy to 2.4 μm in alloy I (see Fig. 4g and h), which can be attributed to the grain boundary pinning by Nb precipitates and/or carbides (e.g., Zener drag and/or solute drag by dissolved Nb) [18]. A similar effect has been observed in microalloyed bainitic steels [71]. The effective grain size further decreased slightly from 2.4 μm in alloy I to 2.1 μm in alloy II, with increased content of B and Nb (0.013%B and 0.3% Nb).

It is well established that the addition of Nb or B can retard the static and dynamic recrystallization of austenite in bainitic steels [72–74]. The synergic effect from the presence of both B and Nb however is expected to be larger than the sum of the separate effects due to Nb+B solute drag [72,74]. Wang et al. [75] attributed this synergistic effect to the formation of Nb-B complexes exerting force on austenite grain boundaries.

Fig. 5(a) presents a BSE-SEM micrograph of the coarsened grain boundary precipitates in alloy II aged at 500 °C for 120 h. Quantitative EDS analysis was carried out to study the relative chemical compositions of the precipitate. Comparing the EDS pattern from spot 3 (precipitate) with EDS pattern from spot 4 (matrix) confirms prominent peaks of Nb, Ti, and Mo in the coarsened precipitate (Fig. 5(b)). The existence of orthorhombic Ni_3Nb precipitates was reported in a previous study on Nb microalloyed 20%

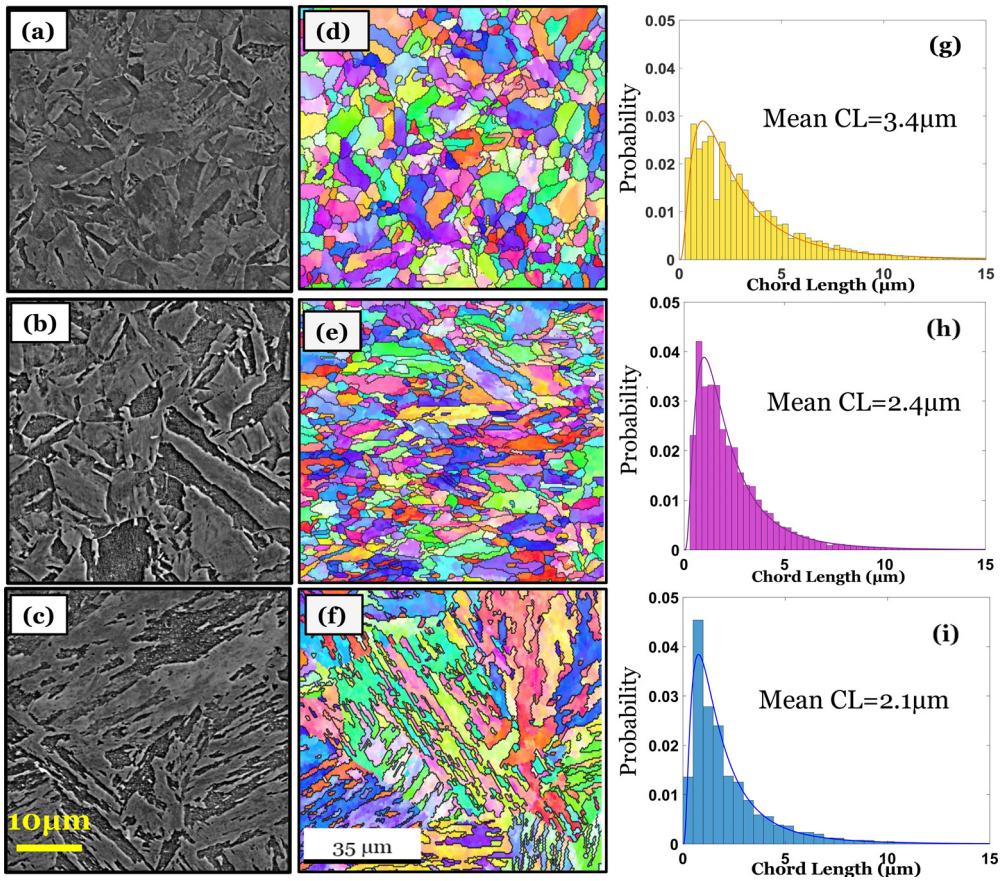

Fig. 4. BSE-SEM micrographs of maraging steels showing morphology of blocks in-as hot forged and solution annealed martensite (a) base alloy (b) alloy I and (c) alloy II. (d–f) Corresponding EBSD-IPF (inverse pole figure) maps of maraging steel alloys depicting high angle grain boundaries (packets and blocks boundaries). (g–i) Chord length distributions (CLD) quantifying the block and packet morphology. Average chord lengths presented in the plot correspond to the average martensite block size.

Ni maraging steels [15]. It was also reported that the reaction of B with the alloying elements in 18% Ni (C350) maraging steels resulted in the formation of Mo- and Ti-rich borides [76]. However, the quantification of the light B element by EDS could be affected by the absorption of boron X-rays by the heavier elements in the martensitic matrix. Therefore, secondary ion mass spectroscopy (SIMS) alpha-ray track etching method (ATE) is necessary for detection and quantification of B at austenite-martensite packet/block boundaries [19,77,78].

Another transformation that can occur simultaneously with dissolution and coarsening of precipitation is the reversion of martensite to austenite [79]. The precipitation reactions occur much more rapidly than the austenite reversion. Thus, substantial hardening can be produced before reversion occurs, where the metastable martensite transforms back to austenite during the later stage of aging (see Fig. 3). This reversion is possible because the diffusion rate of nickel is high enough to permit the system to move towards equilibrium. Equilibrium austenite contributes to the observed overaging and softening in maraging steels. Austenite reversion usually occurs between martensite laths (inter-lath reverted austenite) or at the packets and prior austenite grain boundaries [61,79]; the former was reported to improve the ductility in steels by either blunting the microcracks in the matrix or transformation induced plasticity mechanism (TRIP) [62,80] and the latter was found to cause embrittlement in a 350-grade maraging steel during averaging [61]. Fig. 5c shows XRD patterns of ten selected specimens in the annealed and aged conditions. The spectra mainly consist of peaks of α martensite and/or peaks of γ austenite. Nevertheless, in some conditions (e.g., Aged-500 °C-96 h (Alloy I), Aged-500 °C-120 h (Alloy I)), very small peaks of precipitates are seen and have been marked by black arrows in Fig. 5c. Since the as-annealed samples of the 3 different alloys did not show any austenite peaks, it can be inferred that the austenite present in the aged conditions is most likely reverted austenite, not retained austenite.

The formation of thin areas of lath-like reverted austenite at martensite lath boundaries and pre-austenite grain boundaries in 18% Ni maraging steels after prolonged aging at 500 °C has been reported in prior TEM studies [81]. The austenite content of the samples was estimated as described in Section 2.2, and the results are summarized in Fig. 5d. Comparing the reverted austenite contents in the base alloy, alloy I, and alloy II, it can be seen that the base alloy has a higher amount of reverted austenite compared to the microalloyed alloys for the same aging condition. The volume fraction of austenite in the base alloy increased with aging time until it reached about 19% and remained approximately constant with further aging. The amount of reverted austenite formed in alloy I was found to increase up to about 8.6% after aging for about 72 h, and then decreased to 3% after aging for 120 h (see Table 2). The reduction in the volume fraction of austenite at long aging times can be attributed to the transformation of a small portion of metastable reverted austenite to martensite [82]. This is because the thermal and mechanical stability of reverted austenite is largely governed by its size, chemical compositions (e.g., Ni content), and where it is formed. Alloy II with a higher amount of microalloying elements did not appear to produce any reverted austenite until after 96 h of aging, which then rose to 7% after 120 h aging at 500 °C. These results suggest that B and Nb im-

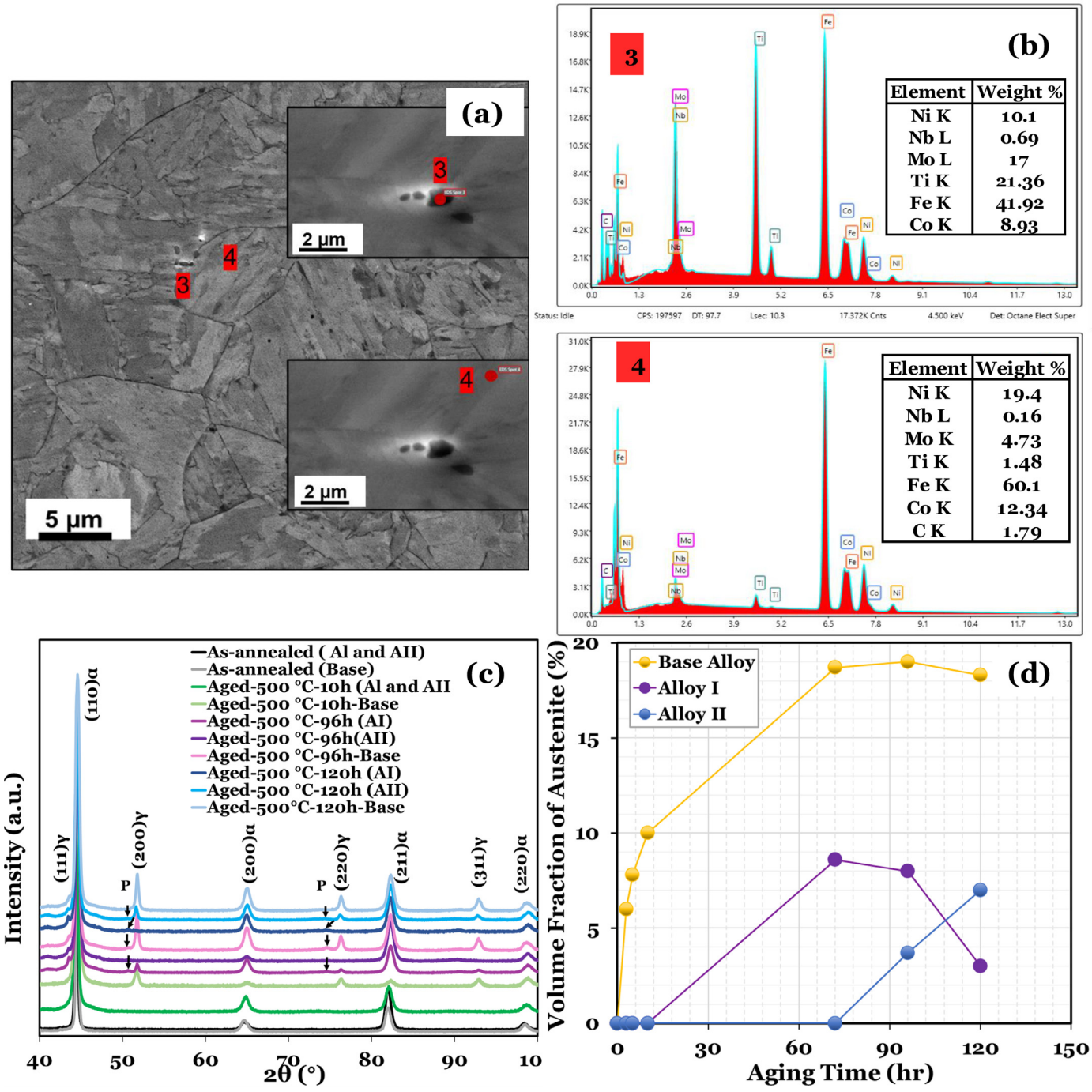

Fig. 5. (a) BSE-SEM micrograph of alloy I aged at 500 °C for 120 h showing grain boundary precipitates. The insets are SE-SEM micrographs where EDS measurements were obtained. (b) EDS spectra of the precipitates (spot 3) and the matrix (spot 4). (c) XRD patterns of 10 selected specimens in as-annealed and aged conditions (AI and AII denote alloy I and alloy II respectively). (d) Evolution of volume fractions (vol%) of reverted austenite as a function of aging time at aging temperature of 500 °C.

pede the formation of reverted austenite at the aging temperature of 500 °C. One possible explanation for this effect is that the nucleation and growth of austenite during aging is governed by the degree of the depletion of Ni from martensite, and coarsening and dissolution of Ni-containing intermetallic precipitates such as Ni_3Nb and Ni_3Ti. Indeed, EDS and TEM analysis have supported the formation of intra lath reverted austenite by the dissolution of Ni_3Ti and Ni_3Mo precipitates in base 18% Ni maraging steels [79,81,83].

3.2. Comparisons between mechanical testing protocols

Since 3 different testing protocols (i.e., conventional hardness, MSS, and tension tests) were conducted on some of the samples, this study provides an opportunity to critically evaluate the relative merits of the different indentation protocols (the tension test results are treated as ground truth in these comparisons). Prior work [50,51,56] has established the following relation between the MSS measured indentation yield strength, σ_{ind}, and the tensile yield strength, σ_y, of polycrystalline metal samples exhibiting close to

Table 2
Mechanical properties of 18% Ni maraging steels studied in this work.

	Aging Time (min)	Hardness (HV_1)	Young's Modulus (E_{alloy}), GPa	Indentation Yield Strength (Y_{ind}), 0.2% offset, MPa	Indentaion Contact Radius at Yield, (a) (μm)	Uniaxial Tensile Yield Strength (Y_S), 0.2% MPa	UTS, MPa	Uniaxial Elongation % Total	Uniform	RA %
	0 (As-annealed)	**320 ± 14**	**170 ± 9**	**1700 ± 80**	**18 ± 1.8**	**827± 76**	**1137± 37**	**18 ± 1.5**	**2.5 ± 0.1**	**70 ± 2.2**
	180	**685 ± 12**	**197 ± 7**	**4620 ± 110**	**32 ± 2.1**	**2358 ± 40**	**2392 ± 45**	**5 ± 1.2**	**1.9 ± 0.1**	**24 ± 4.5**
Base Alloy	**300**	**710 ± 10**	**200 ± 10**	**4692 ± 160**	**32 ± 3.9**	**–**		**–**	**–**	**–**
	600	**690 ± 12**	**200 ± 4**	**4430 ± 158**	**31 ± 3.2**	**–**		**–**	**–**	**–**
	4320	**665 ± 15**	**200 ± 8**	**3996 ± 110**	**27 ± 1.3**	**–**		**–**	**–**	**–**
	5760	**635 ± 13**	**185 ± 10**	**3780 ± 100**	**26 ± 2.9**					
	7200	**620 ± 11**	**185 ± 15**	**3622 ± 72**	**26 ± 2.1**					
	0 (As-annealed)	**345 ± 11**	**175 ± 6**	**1800 ± 190**	**20 ± 1.9**	**889 ± 117**	**1158 ± 31**	**17 ± 0.9**	**2.6 ± 0.1**	**75 ± 0.6**
	180	**715 ± 13**	**200 ± 5**	**4790 ± 198**	**32 ± 1.1**	**2385 ± 72**	**2454 ± 60**	**5 ± 0.9**	**2.1 ± 0.07**	**22 ± 1.2**
	300	**718 ± 8**	**198 ± 4**	**4800 ± 128**	**32 ± 2.9**	**–**		**–**	**–**	**–**
Alloy I	**600**	**720 ± 10**	**208 ± 12**	**4912 ± 86**	**33 ± 0.9**	**2454 ± 9**	**2511 ± 7**	**6 ± 2.2**	**2 ± 0.1**	**31± 16**
	4320	**705 ± 15**	**200 ± 10**	**4824 ± 186**	**32 ± 0.8**	**–**		**–**	**–**	**–**
	5760	**704 ± 12**	**187 ± 20**	**4800 ± 178**	**32 ± 2.3**	**–**		**–**	**–**	**–**
	7200	**680 ± 9**	**189 ± 10**	**4676 ± 148**	**32 ± 0.7**	**–**		**–**	**–**	**–**
	0 (As-annealed)	**340 ± 18**	**170 ± 7**	**1680 ± 150**	**18 ± 2.2**	**847 ± 40**	**1172 ± 13**	**15 ± 0.7**	**2.6 ± 0.1**	**66 ± 0.5**
	180	**710 ± 8**	**200 ± 5**	**4718 ± 156**	**32 ± 0.8**	**2364 ± 80**	**2401 ± 49**	**5 ± 1.5**	**2 ± 0.1**	**29 ± 7.8**
	300	**718 ± 10**	**192 ± 8**	**4816 ± 160**	**32 ± 1.5**	**–**		**–**	**–**	**–**
Alloy II	**600**	**730 ± 11**	**195 ± 9**	**4972 ± 176**	**33 ± 2.1**	**2493 ± 20**	**2536 ± 20**	**4 ± 0.2**	**1.8 ± 0.03**	**18 ± 5.7**
	4320	**726 ± 10**	**202 ± 8**	**4908 ± 182**	**32 ± 2.3**	**–**		**–**	**–**	**–**
	5760	**720 ± 6**	**187 ± 5**	**4890 ± 194**	**32 ± 0.8**	**–**		**–**	**–**	**–**
	7200	**700 ± 8**	**185 ± 16**	**4860 ± 100**	**32 ± 1.7**	**–**		**–**		**–**

isotropic plastic response:

$$\sigma_y \approx \sigma_{ind}/2 \tag{9}$$

Tensile yield strengths can also be estimated from the conventional Vickers hardness measurements. This is accomplished in this study using two different empirical relationships used extensively in current literature. The first relationship was proposed by Tabor [84] based on slip-line field analysis, and is expressed as

$$\sigma_y \approx (HV \times 9.8)/3 \tag{10}$$

where HV is the Vickers hardness in units of kg/mm^2. The second relationship explored in this study was proposed by Pavlina and Tyne [85] based on data gathered on a wide range of non-austenitic steels, and is expressed as

$$\sigma_y \approx -90.7 + 2.876 \times HV \tag{11}$$

It should be noted that Tabor's relation in Eq. (10) was derived for materials exhibiting perfectly plastic response. Since the aged maraging steels studied here show very little hardening, it should be anticipated that Eq. (10) will produce good estimates. On the other hand, Eq. (11) was established for steel alloys with hardness values lower than 632 HV [85]. Therefore, it is also expected to provide good estimates for the maraging steel samples in their as-annealed conditions. It is anticipated that the estimates from Eq. (11) might exhibit higher errors for the much harder aged maraging steel samples.

The accuracies of the estimated values of yield strengths from the 3 different indentation analyses protocols Eqs. (9)–((11)) are visualized in the parity plot shown in Fig. 6. The parity plot reveals a very good agreement between the yield strength values estimated by the MSS protocols with a root mean square error (RMSE) of 2.3%. It is further observed that the MSS estimations outperform the estimations from the Tabor's relation (Eq. (10)), which exhibited an RMSE of 8.5%, and from the Pavlina's relation, which exhibited an RMSE of 24.4%. This is largely because the conventional

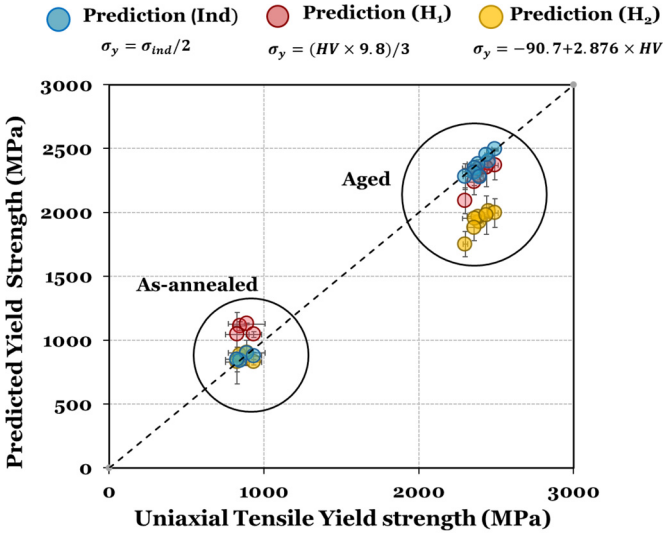

RMSE% (Ind)	RMSE% (H_1)	RMSE% (H_2)
2.3	8.5	24.4

Fig. 6. Parity plot showing the accuracy of the estimated yield strengths of maraging steel alloys studied in this work based on hardness and spherical indentation measurements. H_1 and H_2 denote two different empirical relationships between Vickers hardness and yield strength proposed by Tabor [84] and Pavlina [85], respectively.

approaches measure hardness as the ratio of applied load to the (projected) area of the residual impression left by the indenter after a significant amount of plastic strain has already been applied. As such, hardness measurements do not correspond to the material's tensile yield strength defined close to the initiation of plas-

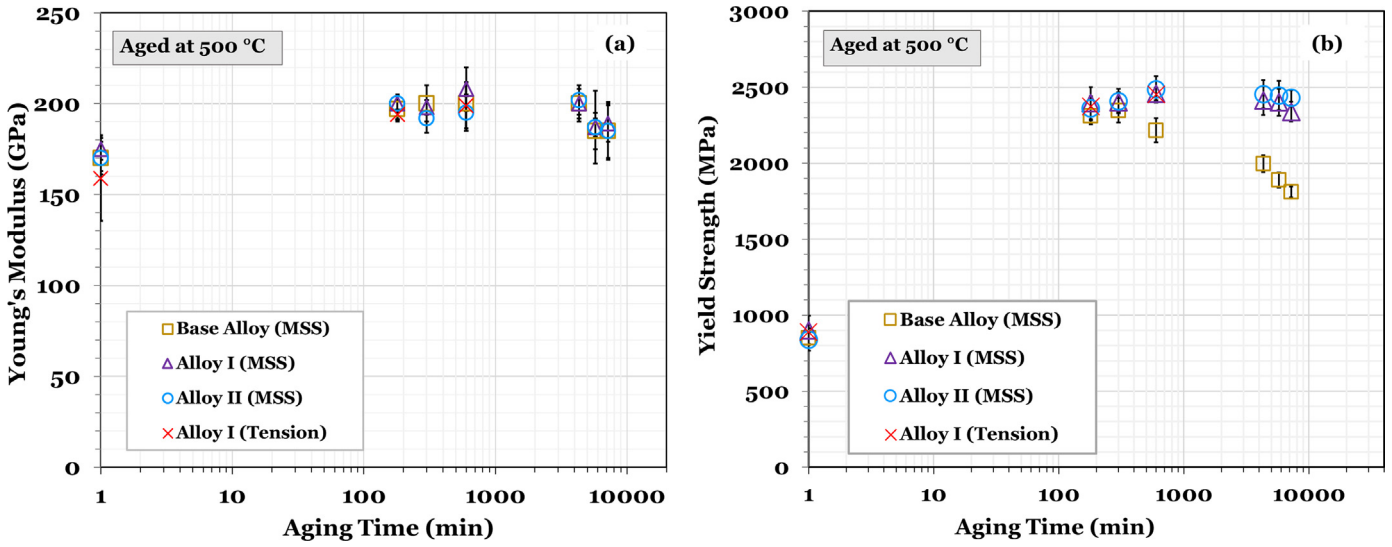

Fig. 7. (a) Young's modulus as a function of aging time for base and microalloyed maraging steels. (b) Estimated tensile yield strength from indentation yield strengths as a function of aging time for base and microalloyed maraging steels. Data was collected using MSS protocols. For comparison, tensile Young's moduli and tensile yield strengths for alloy I in as-annealed and aged conditions (3 and 10h) are marked here by red cross points.

tic deformation in the material. In other words, the conventional hardness measurements correspond to flow stress in the material after a certain (non-standard) amount of plastic deformation has been applied. In contrast, the MSS protocols correlate the tensile yield strength to the indentation yield strength measured very close to the initiation of plastic deformation in the indented sample. The results presented in Fig. 6 indicate that the MSS protocols provide good estimates in both the as-annealed and aged conditions. Furthermore, it should be noted that the MSS protocols require much smaller sample volumes compared to the standardized tension tests.

3.3. Mechanical Behavior of 18% Ni maraging steels

Table 2 summarizes the statistics (means and standard deviations) of the measured mechanical properties of the different maraging steel samples studied in this work. This summary includes the results obtained from ten Vickers hardness tests, six spherical microindentation measurements, and four uniaxial tensile tests (conducted only on selected material conditions) for each sample. The microindentation properties measured in this study included Young's modulus (E_{alloy}), indentation yield strength, and the contact radius at the indentation yield point. The contact radius can be used to estimate the volume of the primary deformation zone under the indenter, approximated as a cylinder of radius a and height $2.4a$ [47,48]. This estimate of the primary indentation zone volume can provide valuable insight into whether the measurement reflects a bulk response. Using this estimated volume, one could estimate the number of grains present in the primary indentation zone volume. For the samples tested in this work, the primary indentation zone volume was found to contain roughly 40–100 martensite blocks. It was observed that the microindentation tests on the as-annealed samples exhibited significantly smaller contact radii at indentation yield (i.e., they engaged a fewer number of martensite packets/blocks in each measurement). This can explain the higher variance in the indentation yield strengths measured in these samples when compared to those measured on the aged samples.

The values of Young's modulus and the estimated yield strengths from the MSS protocols (summarized in Table 2) are compared with each other in Fig. 7. The yield strengths presented in this figure have been estimated using Eq. (9). This figure also provides a visual illustration of the variation of the mechanical properties in both the base and the microalloyed maraging steels as a function of the aging treatments. Note that only a limited number of samples were evaluated in tensile tests (mainly to validate the estimates from the MSS protocols), but the MSS protocols were conducted on many more samples attesting to the high-throughput nature of these protocols. It is seen that the Young's modulus and yield strengths estimated by MSS protocols are in very good agreement with the direct measurements from the standardized tension tests.

It was noted from Fig. 7(a) that the values of Young's modulus increased approximately between 15% and 18% from the as-annealed condition to the aged conditions, with very little variation among the differently aged samples. This is possibly a consequence of the phase transformations occurring in the sample during the aging process, mainly the formation of the intermetallic precipitates. Similar results have been reported in other precipitation-hardened alloys by performing tension and vibration tests [86–88]. The measurements in Fig. 7(a) also suggest a small drop in the values of Young's modulus at longer aging times, although this decrease stays within the standard deviation of the measurements. Also, as expected, the Young's moduli of the alloys are not sensitive to small microalloying additions of B and Nb.

Table 2 and Fig. 7 (b) clearly indicate a dramatic increase in the yield strength of the aged samples compared to the as-annealed samples. Furthermore, they exhibit the characteristic peak-aging response, where the strengthening is optimized for a specific combination of aging temperature and aging time. For the 18% Ni maraging steel (C350), peak-aging is known to occur at around (480–510 °C) [10] when their yield strengths improve to about 2400 MPa (equivalent to 350 Ksi); this strengthening is attributed to the formation of homogeneously dispersed intermetallic precipitates. The indentation measurements reported in Fig. 7(b) are highly consistent with the previous results reported in literature based on standard tension tests.

The effects of microalloying are also clearly seen in the measurements reported in Fig. 7(b). While the peak yield strength (2346 ± 80 MPa) in the base alloy is obtained after 5 h at 500 °C, the peak yield strengths in alloy I and alloy II are attained after 10 h at the same temperature. Moreover, the peak yield strengths of the micro-alloyed samples are slightly higher (2456 ± 43 MPa and

2486 ± 88 MPa, respectively) compared to those obtained in the base alloy. More importantly, the micro-alloyed samples are able to retain their high yield strengths to longer aging times without experiencing over-aging. A very small increase in the yield strength is observed in alloy II compared to alloy I. These observations suggest that B and Nb in the microalloyed steels have enhanced the stability of the intermetallic precipitates, making them difficult to dissolve or coarsen at longer aging time. Therefore, it also seems reasonable that the restriction of the diffusional growth of austenite at lath boundaries in the microalloyed steels is largely influenced by the coarsening kinetics of the precipitates formed. It should be made clear that the individual role of B and Nb could not be determined without further investigation of their various chemistries as the difference in the measured yield strength between the two microalloyed steels is rather small.

As evident from Fig. 7(b), the yield strength values estimated by the MSS protocols are in excellent agreement with the values measured directly in the standard tension tests. The measurements summarized in Table 2 and Fig. 7 indicate that the microalloying additions have enhanced the strength of the maraging steels in both as-annealed and aged conditions with a minor decrease in their ductility. It is however expected that toughness can be degraded by thermal embrittlement during solution annealing in B and Nb microalloyed maraging steels where significant amounts of B and Nb have been added [89]. This effect was originally ascribed to segregation and coarsening of NbB_2 at preaustenite grain boundaries in 18% Ni maraging steels (C350). The highest yield strength and UTS in the present work are attained in alloy II after aging for 10 h.

It is well understood in current literature [7,90–92] that the improvement in the yield strengths from as-annealed conditions to aged conditions seen in precipitation-hardened alloys are a consequence of the formation of nanoscale precipitates and their pinning effect on dislocations. In the microalloyed steels the strength is also predominantly influenced by the contribution from the newly formed precipitates (e.g., Ni_3Nb, NbB, NbTi, NbC Nb, or B containing clusters) in addition to the previously existing ones [7,8,92]. This is largely controlled by the amount of B and/or Nb dissolved in austenite, the tendency of B and Nb to interact with other alloying elements to form borides or other intermetallics, and the segregation of B and/or Nb to austenite grain boundaries either as solutes or in the form of compounds. Yet, precipitation hardening could not be the only contributor to the strength of maraging steels due to the complexity of their microstructures and the high tendency for revision of martensite to austenite during aging. In other words, several additional key factors such as, austenite volume fractions, effective grain size and dislocation density need to be considered in the analysis of the observed changes in the strength of these alloys. More in-depth analysis should be carried out through a combination of TEM, XRD, small-angle neutron scattering (SAX), and APT techniques to understand the effects of dislocation density, chemical composition, size, distribution of precipitate clusters, and the reverted austenite formed in the microalloyed samples. These are out of the scope of the present work.

4. Cost analysis

In our prior work [51], we demonstrated that one key advantage of high throughput spherical microindentation protocols lies in the efficient and cost-effective exploration of the process space. Indeed, the term “high throughput” is being used here to imply acceleration in the process of extracting mechanical properties (e.g., Young’s modulus and yield strength) when compared to conventional approaches. A comparison of cost per sample condition for the MSS protocols, hardness and conventional tensile tests is provided in Fig. 8. For this cost analysis, first, the costs of raw materials purchased, as well as machining and metallography were recorded. Second, the time spent in all the steps involved in these protocols (data collection and data analysis) was recorded and the corresponding costs incurred for the study were estimated. It is clear that the cost of raw materials for both hardness and spherical microindentation tests is identical and the highest raw material cost is associated with the tensile test samples considering that at least 4 tensile samples should be tested for each sample process condition to gather statistically meaningful data. While the cost of machining and polishing 4 round cross-section type tensile samples is approximately $700, the cost of sample preparation for the hardness and spherical microindentation is less than $100.

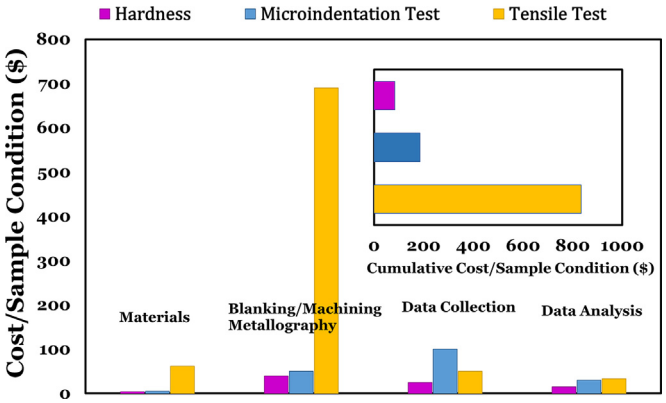

Fig. 8. A comparison of the cost per sample for the hardness test and spherical microindentation protocols (MSS) with the conventional tension tests.

One single indentation test using MSS protocols takes 15–20 min. It is worth mentioning that the data analysis cost for the MSS protocols and conventional tensile protocols are similar. One must pay attention that the total cost of MSS protocols for each process condition is a quarter of the cumulative cost of conventional tensile test protocol, mostly due to the reduction in the sample preparation efforts. The main disadvantage of the MSS protocols in exploration of process space however is that mechanical properties such as ultimate tensile strength (UTS) and ductility estimated in conventional tension tests cannot be retrieved in this manner. It should be noted that while the total cost expended in the hardness test for each process condition is less than the MSS protocols, it does not offer an estimation of Young’s modulus and significantly suffers from lower fidelity in the estimated yield strengths as discussed earlier.

5. Conclusions

This study investigated the influence of combined B and Nb microalloying elements on the microstructure and yield strengths of 18% Ni maraging steels (C350) in as-solution annealed and thermally aged samples (500 °C). A combination of SEM-EDS/EBSD and XRD was used to identify changes in the microstructures due to microalloying elements. The mechanical properties of alloys were evaluated using hardness, high throughput microindentation stress-strain protocols (MSS), and tensile testing. The results are summarized as follows:

1 Reduction in the packet and block size of martensite was observed by EBSD measurements of high angle grain boundaries in as-annealed conditions, which was accompanied by change in the morphologies of these features in the microalloyed steels. This was speculated to be caused by the synergistic roles of B and Nb microalloying elements in changing the M_s temperature and in the retardation of austenite recrystallization during hot forging.

2 The bulk mechanical properties of maraging steels were estimated using high throughput spherical microindentation stress-strain protocols (MSS). The results of these measurements revealed that the presence of Nb and B in the microalloyed maraging steels improved the yield strength of maraging steels. The microindentation results were in excellent agreement with the uniaxial tensile tests conducted on a limited number of sample conditions. Furthermore, delayed coarsening was observed in the microalloyed steels. This effect is largely controlled by the mobility and diffusion rate of elements in the microalloyed steels. It is likely Nb and B microalloying assisted in the development of new precipitate compounds with sluggish mobility for diffusion. A similar retardation effect also is evident from the slower kinetics of the reverted austenite formation in microalloyed steels which contributed to lesser degree of softening in these alloys.

3 The critical comparison between the yield strengths using MSS protocols and conventional tension tests and their corresponding costs demonstrated the viability and merits of MSS protocols for rapid exploration of the process and chemistry spaces. Obviously, the MSS protocols offer attractive alternatives that save money and time compared to the conventional uniaxial testing, and much higher fidelity in the estimation of yield strength compared to the hardness test.

Declaration of Competing Interest

The authors declare that they have no known competing financial interests or personal relationships that could have appeared to influence the work reported in this paper.

Acknowledgments

The authors gratefully acknowledge support from NSF 1761406 and the Boeing Company. We also would like to thank the members of IEN/IMAT Materials Characterization Facility at Georgia Institute of Technology. The authors are thankful to Mr. David Tavakoli and Mr. Steven J. Koskey from the Georgia Institute of Technology and Dr. Bruno Zamorano from the Boeing Co. for their supports.

References

[1] R. Tewari, et al., Precipitation in 18 wt% Ni maraging steel of grade 350, Acta Mater. 48 (5) (2000) 1187–1200.
[2] U.K. Viswanathan, R. Kishore, M.K. Asundi, Effect of thermal cycling on the mechanical properties of 350-grade maraging steel, Metall. Mater. Trans. A 27 (3) (1996) 757–761.
[3] B.Z. Weiss, Maraging steels—structure, properties and applications, Spec. Steel. Hard Mater. (1983) 35–54.
[4] A.M. Hall, C.J. Slunder, The Metallurgy, Behavior, and Application of the 18-Percent Nickel Maraging Steels, National Aeronautics and Space Administration, Washington, 1968 1968: Washington, National Aeronautics and Space Administration, 1968.
[5] V. Gray, et al., Precipitation in a novel maraging steel F1E: A study of austenitization and aging using small angle neutron scattering, Mater. Charact. 129 (2017) 270–281.
[6] Y. He, et al., Strengthening and toughening of a 2800-MPa grade maraging steel, Mater. Lett. 56 (5) (2002) 763–769.
[7] M. Niu, et al., Precipitate evolution and strengthening behavior during aging process in a 2.5 GPa grade maraging steel, Acta Mater. 179 (2019) 296–307.
[8] U.K. Viswanathan, G.K. Dey, M.K. Asundi, Precipitation hardening in 350 grade maraging steel, Metall. Trans. A 24 (11) (1993) 2429–2442.
[9] O. Moshka, et al., Addressing the issue of precipitates in maraging steels - Unambiguous answer, Mater. Sci. Eng. A (2015).
[10] S. Floreen, The physical metallurgy of maraging steels, Metall. Rev. 13 (1) (1968) 115–128.
[11] F. Qian, J. Sharp, W.M. Rainforth, Microstructural evolution of Mn-based maraging steels and their influences on mechanical properties, Mater. Sci. Eng. A 674 (2016) 286–298.
[12] G.M. Castro Güiza, C.A.S. Oliveira, Microstructural changes produced by hot forging in a C300 Maraging Steel, Mater. Sci. Eng. A 655 (2016) 142–151.
[13] J. Tian, et al., A new maraging stainless steel with excellent strength-toughness-corrosion synergy, Materials 10 (11) (2017) 1293 (Basel, Switzerland).
[14] D.G. Lee, et al., The influence of niobium and aging treatment in the 18% Ni maraging steel, J. Mater. Proc. Technol. 162-163 (2005) 342–349.
[15] M. Ahmed, et al., Reclamation and additional alloying of 18Ni(350) maraging steel, J. Mater. Eng. Perform. 3 (3) (1994) 386–392.
[16] S.B. Nizhnik, G.I. Usikova, Investigation of structural conditions for improving the characteristics of strength, plasticity, and fracture toughness of maraging steels, Strength Mater. 32 (2) (2000) 141–148.
[17] P.P. Senthil, et al., Influence of niobium microalloying on the microstructure and mechanical properties of high carbon nano bainitic steel, Proc.Struct. Integr. 14 (2019) 729–737.
[18] T.N. Baker, Microalloyed steels, Ironmak. Steelmak. 43 (4) (2016) 264–307.
[19] T. Hara, et al., Role of combined addition of niobium and boron and of molybdenum and boron on hardnenability in low carbon steels, ISIJ Int. 44 (8) (2004) 1431–1440.
[20] K.R. Lottey, M. Militzer, Microstructure evolution in fine-grained microalloyed steels, Mater. Sci. Forum 500-501 (2005) 347–354.
[21] H. Tamehiro, et al., Optimum microalloying of niobium and boron in HSLA steel for thermomechanical processing, Trans. Iron Steel Inst. Jpn. 27 (2) (1987) 120–129.
[22] A.J. Deardo, Niobium in modern steels, Int. Mater. Rev. 48 (6) (2003) 371–402.
[23] B.M. Kapadia, Effect of boron additions on the toughness of heat-treated low-alloy steels, J. Heat Treat. 5 (1) (1987) 41–53.
[24] A.A. Azarkevich, L.V. Kovalenko, V.M. Krasnopolskii, The optimum content of boron in steel, Metal Sci. Heat Treat. 37 (1) (1995) 22–24.
[25] Y.J. Li, et al., Atomic scale investigation of non-equilibrium segregation of boron in a quenched Mo-free martensitic steel, Ultramicroscopy 159 (2015) 240–247.
[26] A. Khosravani, A. Cecen, S.R. Kalidindi, Development of high throughput assays for establishing process-structure-property linkages in multiphase polycrystalline metals: application to dual-phase steels, Acta Mater. 123 (2017) 55–69.
[27] X. Gong, et al., High throughput assays for additively manufactured Ti-Ni alloys based on compositional gradients and spherical indentation, Integr. Mater. Manufact. Innov. (2017).
[28] Z. Li, et al., Combinatorial metallurgical synthesis and processing of high-entropy alloys, J. Mater. Res. 33 (19) (2018) 3156–3169.
[29] C. Baron, H. Springer, D. Raabe, Combinatorial screening of the microstructure–property relationships for Fe–B–X stiff, light, strong and ductile steels, Mater. Des. 112 (2016) 131–139.
[30] S. Ding, et al., Combinatorial development of bulk metallic glasses, Nat. Mater. 13 (5) (2014) 494–500.
[31] R. Potyrailo, et al., Combinatorial and high-throughput screening of materials libraries: review of state of the art, ACS Comb. Sci. 13 (6) (2011) 579–633.
[32] H. Springer, D. Raabe, Rapid alloy prototyping: Compositional and thermo-mechanical high throughput bulk combinatorial design of structural materials based on the example of 30Mn–1.2C–xAl triplex steels, Acta Mater. 60 (12) (2012) 4950–4959.
[33] R.F. Bishop, R. Hill, N.F. Mott, The theory of indentation and hardness tests, Proc. Phys. Soc. 57 (3) (1945) 147–159.
[34] W.C. Oliver, G.M. Pharr, An improved technique for determining hardness and elastic modulus using load and displacement sensing indentation experiments, J. Mater. Res. 7 (6) (1992) 1564–1583.
[35] G.M. Pharr, W.C. Oliver, Measurement of thin film mechanical properties using nanoindentation, MRS Bull. 17 (7) (1992) 28–33.
[36] I.S. Choi, et al., Mechanics of indentation of plastically graded materials—II: experiments on nanocrystalline alloys with grain size gradients, J. Mech. Phys. Solid. 56 (1) (2008) 172–183.
[37] T. Ohmura, K. Tsuzaki, S. Matsuoka, Nanohardness measurement of high-purity Fe–C martensite, Scr. Mater. 45 (8) (2001) 889–894.
[38] L. Zhang, et al., Characterization of local deformation behavior of Fe–Ni lenticular martensite by nanoindentation, Mater. Sci. Eng. A 527 (7) (2010) 1869–1874.
[39] E.I. Galindo-Nava, W.M. Rainforth, P.E.J. Rivera-Díaz-del-Castillo, Predicting microstructure and strength of maraging steels: elemental optimisation, Acta Mater. 117 (2016) 270–285.
[40] J.S. Zhang, et al., Ageing behaviour of spray-deposited 18Ni(250) maraging steel + 10 vol.% Al_2O_3 particulate-reinforced metal matrix composites, Mater. Sci. Eng. A 225 (1) (1997) 96–104.
[41] S. Parvinian, et al., Through-thickness strain gradient in a Hot-rolled Al-Mg alloy obtained by Nanoindentation and glancing angle X-Ray diffraction, J. Mater. Eng. Perform. 28 (11) (2019) 6897–6903.
[42] G.M. Pharr, E.G. Herbert, Y. Gao, The indentation size effect: a critical examination of experimental observations and mechanistic interpretations, Ann. Rev. Mater. Res. 40 (1) (2010) 271–292.
[43] J.G. Swadener, E.P. George, G.M. Pharr, The correlation of the indentation size effect measured with indenters of various shapes, J. Mech. Phys. Solid. 50 (4) (2002) 681–694.
[44] J. Gong, J. Wu, Z. Guan, Examination of the indentation size effect in low-load vickers hardness testing of ceramics, J. Eur. Ceram. Soc. 19 (15) (1999) 2625–2631.
[45] Sargent, P.M., Use of the Indentation Size Effect on Microhardness for Materials Characterization, P.J. Blau and B.R. Lawn, Editors. 1985, ASTM International: West Conshohocken, PA. p. 160–174.
[46] K. Sangwal, B. Surowska, P. Błaziak, Analysis of the indentation size effect in the microhardness measurement of some cobalt-based alloys, Mater. Chem. Phys. 77 (2) (2003) 511–520.

[47] S. Pathak, S.R. Kalidindi, Spherical nanoindentation stress-strain curves, Mater. Sci. Eng. R Rep. (2015).
[48] S.R. Kalidindi, S. Pathak, Determination of the effective zero-point and the extraction of spherical nanoindentation stress-strain curves, Acta Mater. (2008).
[49] J.S. Weaver, S.R. Kalidindi, Mechanical characterization of Ti-6Al-4V titanium alloy at multiple length scales using spherical indentation stress-strain measurements, Mater. Des. (2016).
[50] D.K. Patel, S.R. Kalidindi, Correlation of spherical nanoindentation stress-strain curves to simple compression stress-strain curves for elastic-plastic isotropic materials using finite element models, Acta Mater. (2016).
[51] J.S. Weaver, et al., High throughput exploration of process-property linkages in Al-6061 using instrumented spherical microindentation and microstructurally graded samples, Integrat. Mater. Manufact. Innovat. (2016).
[52] V.X. Lima Filho, I.F. Barros, H.F.G.d. Abreu, Influence of solution annealing on microstructure and mechanical properties of Maraging 300 steel, Mater. Res. 20 (1) (2017) 10–14 (Sao Carlos, Online).
[53] G. Singh, M. Ghosh, Study on *precipitation harden*ing of C 250 *grade maraging st*eel, Trans. Indian Inst. Metal., 70, 2017.
[54] S. Parvinian, et al., High-*throughput exploration of the process s*pace in 18% Ni (350) *maraging steels via spherical indentation stress–strain protocols and Gau*ssian *p*rocess *m*odels, Integrat. Mater. Manufact. Innovat. (2020).
[55] ASTM E975-13Standard Practice for X-Ray Determination of Retained Austenite in Steel with Near Random Crystallographic Orientation, ASTM International, West Conshohocken, PA, 2013 www.astm.org.
[56] A. Iskakov, et al., Application of spherical indentation and the materials knowledge system framework to establishing microstructure-yield strength linkages from carbon steel scoops excised from high-temperature exposed components, Acta Mater. 144 (2018) 758–767.
[57] A.C. Fischer-Cripps, The Hertzian contact surface, J. Mater. Sci. 34 (1) (1999) 129–137.
[58] B.R. Donohue, A. Ambrus, S.R. Kalidindi, Critical evaluation of the indentation data analyses methods for the extraction of isotropic uniaxial mechanical properties using finite element models, Acta Mater. 60 (9) (2012) 3943–3952.
[59] S.R. Kalidindi, S. Pathak, Determination of the effective zero-point and the extraction of spherical nanoindentation stress–strain curves, Acta Mater. 56 (14) (2008) 3523–3532.
[60] L. Morsdorf, et al., 3D structural and atomic-scale analysis of lath martensite: effect of the transformation sequence, Acta Mater. 95 (2015) 366–377.
[61] U.K. Viswanathan, G.K. Dey, V. Sethumadhavan, Effects of austenite reversion during overageing on the mechanical properties of 18 Ni (350) maraging steel, Mater. Sci. Eng. A 398 (1) (2005) 367–372.
[62] T. Yasuno, et al., Toughening of maraging steel by retained austenite, Tetsu Hagane 78 (12) (1992) 1824–1830.
[63] M.K. El-Fawkhry, et al., Development of maraging steel with retained austenite in martensite matrix, Mater. Today Proc. 2 (2015) S711–S714.
[64] L.G.d. Carvalho, et al., Kinetics of martensite reversion to austenite during overaging in a maraging 350 Steel, ISIJ Int. 59 (6) (2019) 1119–1127.
[65] S. Morito, et al., Effect of block size on the strength of lath martensite in low carbon steels, Mater. Sci. Eng. A 438-440 (2006) 237–240.
[66] J.W. Morris, The influence of grain size on the mechanical properties ofsteel, Lawrence Berkeley Natl. Lab. (2001).
[67] C. Capdevila, F.G. Caballero, C. García De Andrés, Analysis of effect of alloying elements on martensite start temperature of steels, Mater. Sci. Technol. 19 (5) (2003) 581–586.
[68] C. Capdevila, F. Caballero, C.G. de Andrés, Analysis of effect of alloying elements on martensite start temperature of steels, Mater. Sci. Technol. 19 (2003) 581–586.
[69] R. Song, et al., Grain boundary characterization and grain size measurement in an ultrafine-grained steel, Int. J. Mater. Res. Former. Z. Fuer Metall. 95 (2004) 513–517.
[70] D.M. Turner, S.R. Niezgoda, S.R. Kalidindi, Efficient computation of the angularly resolved chord length distributions and lineal path functions in large microstructure datasets, Modell. Simul. Mater. Sci. Eng. 24 (7) (2016) 075002.
[71] H. Mohrbacher, et al., in: MoNb-Based Alloying Concepts for Low-Carbon Bainitic Steels, Springer Berlin Heidelberg, Berlin, Heidelberg, 2011, pp. 289–301. Berlin, Heidelberg.
[72] H. Mohrbacher, Fundamentals and applications of Mo and Nb alloying in high performance steels, in: Proceedings of the Second International Symposium on Fundamentals and Applications of Mo and Nb Alloying in High Performance Steels, 2, 2013.
[73] S.F. Medina, J.E. Mancilla, Influence of alloying elements in solution on static recrystallization kinetics of hot deformed steels, ISIJ Int. 36 (8) (1996) 1063–1069.
[74] A. Larrañaga-Otegui, et al., Austenite static recrystallization kinetics in microalloyed B steels, Metall. Mater. Trans. A 47 (6) (2016) 3150–3164.
[75] X.M. Wang, X.L. He, Effect of boron addition on structure and properties of low carbon bainitic steels, ISIJ Int. 42 (2002) S38–S46 Suppl.
[76] T.B. Sercombe, Sintering of freeformed maraging steel with boron additions, Mater. Sci. Eng. A 363 (1) (2003) 242–252.
[77] J.-B. Seol, et al., Atom probe tomography and nano secondary ion mass spectroscopy investigation of the segregation of boron at austenite grain boundaries in 0.5 wt.% carbon steels, Metal. Mater. Int. 17 (2011) 413–416.
[78] G. Da Rosa, et al., Grain-boundary segregation of boron in high-strength steel studied by nano-SIMS and atom probe tomography, Acta Mater. 182 (2020) 226–234.
[79] M. Farooque, et al., The formation of reverted austenite in 18% Ni 350 grade maraging steel, J. Mater. Sci. J. Mater. Sci. 33 (1998) 2927–2930.
[80] M.M. Wang, et al., Spectral TRIP enables ductile 1.1 GPa martensite, Acta Mater. 111 (2016) 262–272.
[81] X. Li, Z. Yin, Reverted austenite during aging in 18Ni(350) maraging steel, Mater. Lett. 24 (4) (1995) 239–242.
[82] R. Hossain, et al., Stability of retained austenite in high carbon steel under compressive stress: an investigation from macro to nano scale, Sci. Rep. 6 (1) (2016) 34958.
[83] B. Yan, et al., The Effect of precipitate evolution on austenite grain growth in RAFM steel, Materials 10 (2017) 1017.
[84] D. Tabor, The hardness of solids, Rev. Phys. Technol. 1 (3) (1970) 145–179.
[85] E.J. Pavlina, C.J. Van Tyne, Correlation of yield strength and tensile strength with hardness for steels, J. Mater. Eng. Perform. 17 (6) (2008) 888–893.
[86] X. Huang, et al., The influence of precipitation transformation on Young's modulus and strengthening mechanism of a Cu–Be binary alloy, Mater. Sci. Eng. A 772 (2019) 138592.
[87] A. Szczepaniak, et al., Strengthening Fe – TiB2 based high modulus steels by precipitations, Mater. Des. 124 (2017) 183–193.
[88] P. Behjati, H. Vahid Dastjerdi, R. Mahdavi, Influence of ageing process on sound velocity in C17200 copper–beryllium alloy, J. Alloy. Compd. 505 (2) (2010) 739–742.
[89] T. Yasuno, K. Kuribayashi, T. Hasegawa, Toughening of 18%Ni maraging steel by the combined addition of Nb and B, Tetsu Hagane 84 (11) (1998) 817–822.
[90] R. Schnitzer, S. Zinner, H. Leitner, Modeling of the yield strength of a stainless maraging steel, Scr. Mater. 62 (5) (2010) 286–289.
[91] W.M. John, Particle strengthening of metals and alloys, Mater. Sci. Technol. 13 (8) (1997) 705.
[92] V. Vasudevan, S. Kim, C. Wayman, Precipitation reactions and strengthening behavior in 18 Wt Pct nickel maraging steels, Metall. Trans. 21 (1990) 2655–2668.